

CMB maps lensed by cosmological structures: Simulations and statistical analysis

L. Antón, P. Cerdá-Durán, V. Quilis and D. Sáez

*Departamento de Astronomía y Astrofísica, Universidad de Valencia, 46100, Burjassot,
Valencia, Spain*

diego.saez@uv.es

ABSTRACT

A method for ray-tracing through n-body simulations has been recently proposed. It is based on a periodic universe covered by simulation boxes. Photons move along appropriate directions to avoid periodicity effects. Here, an improved version of this method is applied to simulate lensed CMB maps and maps of lens deformations. Particle mesh n-body simulations with appropriate boxes and resolutions are used to evolve the nonlinear inhomogeneities until present time. The resulting maps are statistically analyzed to look for deviations from Gaussianity. These deviations are measured –for the first time– using correlations for configurations of n directions ($n \leq 6$). A wide range of angular scales are considered. Some interesting prospects are outlined.

Subject headings: cosmic microwave background — cosmology: theory — large scale structure of universe

1. Introduction

In this paper, lensed and unlensed maps of the Cosmic Microwave Background (CMB) temperature distribution are simulated and analyzed. We are particularly interested in estimating deviations with respect to Gaussianity. Any calculation in this field requires the previous assumption of both a background universe and a distribution of cosmological inhomogeneities. Taking into account results from the analysis of the WMAP (Wilkinson Microwave Anisotropy Probe) first year data (Bennet et al. 2003), the cosmological background is assumed to be an inflationary cold dark matter universe with cosmological constant

and reionization. The reduced Hubble constant is $h = 10^{-2}H_0 = 0.71$ (H_0 being the Hubble constant in units of $Km s^{-1}Mpc^{-1}$), the density parameters corresponding to baryons, dark matter, and vacuum, are $\Omega_b = 0.04$, $\Omega_d = 0.23$ and $\Omega_\Lambda = 0.73$, respectively, the total density parameter is $\Omega = \Omega_b + \Omega_d + \Omega_\Lambda = 1$ (inflationary flat universe), and the matter density parameter is $\Omega_m = \Omega_b + \Omega_d = 0.27$. A total reionization is assumed at redshift $z = 17$. Cosmological tensor perturbations are absent, whereas the scalar ones are adiabatic energy fluctuations with a Zel'dovich spectrum and a Gaussian distribution. Under all these assumptions, the CMBFAST code (Seljak & Zaldarriaga 1996) has been used to get the angular power spectrum of the CMB in the absence of lensing (primary anisotropy plus the integrated Sachs-Wolfe effect and reionization imprints; hereafter dominant anisotropy) and then, a method based on the Fast Fourier Transform (Sáez et al. 1996) is used to simulate unlensed Gaussian maps of the temperature contrast Δ_D corresponding to dominant anisotropy. These maps do not appear to be fully Gaussian because they are generated and analyzed by means of discretized numerical processes. Deviations from Gaussianity are studied below in an appropriate interval of small angular scales. The simulated maps of dominant anisotropy are deformed by lensing.

The CMB is lensed by cosmological objects evolving in the linear, mildly nonlinear, and strongly nonlinear regimes. All these structures deviate the propagation direction of the CMB photons. The resulting deviations deform the unlensed maps to produce lensed ones. Linear and mildly nonlinear structures can be studied by using analytical or semi-analytical methods and, consequently, lens deformations caused by this kind of inhomogeneities can be calculated without numerical n-body simulations of structure formation; however, the lens effect of strongly nonlinear structures, as galaxy clusters and substructures, is often studied by using ray-tracing through n-body simulations. The history of the researches about lensing and its status at the end of the last decade can be found in Jain, Seljak, & White (2000); in that paper, the authors gave very exhaustive bibliography and described and used the classic ray-tracing method based on multiple plane projections. Afterwards, another interesting method was proposed by White & Hu (2001). This second method is based on many independent simulations, with different boxes and resolutions, tiling the photon trajectories. Finally, a third method using an unique simulation has been recently proposed (Cerdá-Durán et al. 2004). It is used here after some improvements. The main features and advantages of this last method are now pointed out.

The use of a n-body simulation constraint us to work in a periodic universe tiled by identical boxes. Photons move in this unrealistic periodic universe and the effect of periodicity is important. It magnifies lens deviations. This magnification depends on the observation direction and, fortunately, there are directions leading to negligible periodicity effects. They are hereafter called *preferred directions*. In order to understand the existence

of these directions (minimizing periodicity effects) let us consider the two-dimensional (2D) sketch displayed in Fig. 1, where squares tile a bi-dimensional universe, O is the observer, circles are clusters, and lines are photon trajectories. If photons move parallel to the square edges (dashed line), they enter neighbouring squares through the same point and pass near the same structures in all the squares; hence, lens deviations caused by repeated structures add and, consequently, a wrong magnified accumulative lens effect arises. Now, the question is: what happens if photons follow the solid line? In such a case, photons enter successive boxes through different points separated a distance L as that represented in Fig. 1. For appropriate values of the angle ϕ , distance L becomes greater than: (i) the distance at which clusters produce relevant deviations of the photon directions (a few Megaparsecs), and (ii) the spatial scales of significant cluster correlations ($\sim 30 Mpc$); hence, distances $L > 30 Mpc$ suffice to ensure that photons are deviated by distinct independent clusters located in different uncorrelated regions. Since there are structures more extended than clusters in the n-body simulation, a cutoff avoiding all the spatial scales larger than a scale $L_{cut} \simeq L$ is performed in the peculiar potential given by the n-body simulation. It is worthwhile to notice that the simulation uses all the involved scales to calculate the gravitational potential and to evolve particles. The scales greater than L_{cut} are subtracted from the resulting gravitational potential only to estimate lensing. Using the proposed cutoff, CMB photons are lensed by distinct structures in successive boxes and, furthermore, too large scales which are not well described in our simulation box are eliminated. Finally, it is worthwhile to remark that, as a result of periodicity, there are no discontinuities in the points where photons pass from a box to the next one (hereafter called *crossing points*); as discussed in the next paragraph, this fact can be important in order to get a good estimate of lens deviations.

Roto-translations of the squares could be used to avoid the effects of periodicity. If photons move through the dashed line (parallel to the square edges) but a translation of length L is performed when photons arrive to the crossing points; then, photons are lensed by different clusters in distinct boxes (as it occurs for the preferred directions in our procedure); nevertheless, roto-translations produce unavoidable discontinuities in the crossing points. It is due to the fact that the photon arrives to an edge at a certain point P, but it enters the next square –after translation– through a different point Q. The same occurs for rotations and roto-translations and, also, when we use the tiling method proposed by White & Hu (2001), in which, different simulations are performed in each square. These discontinuities are numerical artifacts and its importance cannot be neglected *a priori*.

If the 3D case is considered, the situation is analogous; then, our universe is covered by boxes and the trajectories parallel to edges are not appropriate to estimate true lens deviations minimizing periodicity effects; nevertheless, if an appropriate observation direction is chosen and a cutoff is consistently performed, a large number of boxes can be crossed

through different independent regions without reentering in the zone where the CMB photon moved initially. Let us discuss this fact in detail. A Cartesian coordinate system is considered in this discussion; its origin O is placed at the center of a box, and the axis are parallel to the box edges whose length is L_{box} . The observer is at O and \vec{n} is the unit vector in the direction of a line of sight. This vector can be written either in terms of spherical coordinates θ and ϕ or in the form $\vec{n} = (\cos \alpha, \cos \beta, \cos \gamma)$, where α , β , and γ are the angles formed by \vec{n} and the x, y, and z-axis, respectively. This second notation is the most appropriate for us. Evidently, if a CMB photon go through the x-axis a distance OX , then, it advances the distances $OY = (\cos \beta / \cos \alpha)OX$ and $OZ = (\cos \gamma / \cos \alpha)OX$ along the y and z-axis, respectively. Hence, if the photon crosses n boxes in the direction of the x-axis, it crosses $m = (\cos \beta / \cos \alpha)n$ ($p = (\cos \gamma / \cos \alpha)n$) in the direction y (z). On account of these considerations, preferred directions are easily obtained; as an example, for quantities $n = 5$, $m = 1$, $p = 1 + (1/6)$, and $L = 256 \text{ Mpc}$, if the photon crosses a box face orthogonal to the x-axis at point M and it crosses the successive parallel face at point N , the distance MN in the y-z plane is $L = L_{box}[(m/n)^2 + ((p-1)/n)^2]^{1/2} = 51.9 \text{ Mpc}$ and, furthermore, the photon only return to the starting point after crossing $n/(p-1) = 30$ boxes in the x direction; namely, after going through a comoving distance of $\sim 8000 \text{ Mpc}$ in the preferred direction, which is the distance from $z \sim 5.2$ to $z = 0$ in the background universe under consideration. At redshift $z = 5.2$ the box size (256 Mpc) subtends an angle of ~ 1.83 degrees. Since the observer is located at the center of a box, for a $1.83^\circ \times 1.83^\circ$ map, the initial photon positions at $z = 5.2$ –involved in our ray-tracing procedure– are all located inside the same initial box and on a sphere having a comoving radius of $\sim 8000 \text{ Mpc}$. For greater maps, initial positions cover various boxes and, consequently, the resulting maps would have the imprint of the spatial periodicity. That is true even if each photon crosses independent regions through a direction close to the preferred one. A large enough number of small $1.83^\circ \times 1.83^\circ$ maps allow us a good estimate of correlations for angles smaller than $\sim 0.25^\circ$ (ℓ greater than ~ 800).

Units are chosen in such a way that $c = 8\pi G = 1$, where c is the speed of light and G the gravitation constant. Whatever quantity "A" may be, A_L and A_0 stand for the A values on the last scattering surface and at present time, respectively. The scale factor is $a(t)$, where t is the cosmological time, and its present value, a_0 , is assumed to be unity, which is always possible in flat universes.

2. Formalism

Since lensing produces changes in the propagation direction of the CMB photons, the temperature contrast Δ observed in the \vec{n} direction is the dominant temperature contrast Δ_D corresponding to another direction \vec{n}_0 ($\Delta(\vec{n}) = \Delta_D(\vec{n}_0)$). The difference $\vec{\delta} = \vec{n}_0 - \vec{n}$ is the deviation due to lensing; hence,

$$\Delta(\vec{n}) = \Delta_D(\vec{n} + \vec{\delta}) \quad (1)$$

The deviation field due to cosmological structures is (Seljak 1996):

$$\vec{\delta} = -2 \int_{\lambda_L}^{\lambda_0} W(\lambda) \vec{\nabla}_{\perp} \phi \, d\lambda, \quad (2)$$

where $\vec{\nabla}_{\perp} \phi = -\vec{n} \wedge \vec{n} \wedge \vec{\nabla} \phi$ is the transverse gradient of the peculiar gravitational potential, and $W(\lambda) = (\lambda_L - \lambda)/\lambda_L$. The variable λ is

$$\lambda(a) = H_0^{-1} \int_a^1 \frac{db}{(\Omega_{m0}b + \Omega_{\Lambda}b^4)^{1/2}}. \quad (3)$$

The integral in the r.h.s. of Eq. (2) is to be evaluated along the background null geodesics.

The peculiar potential ϕ involved in Eq. (2) can be decomposed in the form $\phi = \phi_1 + \phi_2$, where ϕ_1 (ϕ_2) is the potential created by the scales smaller (greater) than L_{cut} . For appropriate values of the separation scale L_{cut} , potentials ϕ_1 and ϕ_2 are independent and, furthermore, ϕ_1 can be obtained with a n-body simulation in a box having a size larger than L_{cut} (a few hundreds of Megaparsecs), whereas the potential ϕ_2 can be simulated in a very big box (a few thousands of Megaparsecs) by using the potential of the linear approximation. There are two kinds of boxes tiling the universe, which are crossed by the same null geodesics. $L_{cut} = 60 \text{ Mpc}$ is a good choice as it is discussed below. The total deviation given by Eq. (2) is the addition of the deviations corresponding to the independent potentials ϕ_1 and ϕ_2 .

In the potential approximation (Martínez-González et al. 1990), which is valid for linear inhomogeneities no larger than the horizon scale and also for nonlinear structures, function ϕ satisfies the equation:

$$\Delta\phi = \frac{1}{2}a^2(\rho - \rho_{m0}), \quad (4)$$

where $\rho_{m0} = \Omega_{m0}\rho_{crit}$ is the background energy density for matter. In the case of clusters, substructures and scales smaller than L_{cut} , the peculiar potential ϕ_1 is given by an appropriate n-body simulation –based on Eq. (4)– at each time step. As it is well known, the potential ϕ_2 created by linear scales larger than L_{cut} has a constant spatial profile and it is proportional the ratio $D_1(a)/a$, where $D_1(a)$ is the growing mode of the scalar density

fluctuations in the model under consideration (see Peebles (1980) and also Fullana & Sáez (2000)). At present time, the spatial scales producing significant lens correlations at angular scales $\alpha \leq 0.25^\circ$ ($\ell \geq 800$) are not larger than the horizon scale ($3000h^{-1} \text{ Mpc}$) and, consequently, either Eq. (4) or its Fourier counterpart can be used to get ϕ_{20} ; namely, to get the constant spatial ϕ_2 profile. For any of the above potentials, the integral (2) is performed on the background null geodesics

$$x^i = x_o^i + \lambda(a)n^i , \quad (5)$$

passing by the point O where our observer is located and having directions \vec{n} .

The chosen \vec{n} directions point towards the region of the sky we are mapping and cover the map in an appropriate way. We always use a regular coverage. These directions define the map nodes where temperature contrasts are calculated and, consequently, they fix the map resolution and its size. Once the lines of sight are chosen, unlensed CMB maps of dominant anisotropy $\Delta_D(\vec{n})$ (hereafter U maps) are built up by using the method described by Sáez et al. (1996) (see §1); hence, the directions \vec{n} point toward the nodes of the U maps. The lens deviations of the potentials ϕ_1 and ϕ_2 are calculated for the same directions (map nodes) by means of Eq. (2). These partial deviations are added to get the total deviation, which is used to obtain the direction $\vec{n} + \vec{\delta}$; finally, the exact Eq. (1) is used –without any approximation– to calculate a lensed $\Delta(\vec{n})$ map (hereafter L map). Since the direction $\vec{n} + \vec{\delta}$ does not point –in general– towards a node of the U map, appropriate interpolation methods are necessary to get the quantity $\Delta_D(\vec{n} + \vec{\delta})$ involved in Eq. (1). The U maps to be lensed has a resolution close to one arcminute ($\ell \sim 10000$) and, consequently, interpolations are performed on scales much smaller than the angular scales affected by lensing ($800 \leq \ell \leq 3000$, see below). The high resolution of the U maps allow us the use of linear interpolation (which does not produce deviations from Gaussianity), and also nonlinear interpolation based on splines, which would only alter Gaussianity for $\ell \sim 10000$. Finally, the map of the differences $\Delta(\vec{n}) - \Delta_D(\vec{n})$ is also calculated (hereafter D map); it is the difference (node by node) between a L maps and its associated U map; hence, relation L=U+D has an evident meaning.

Either the n-body potential or the linear one can be used to calculate the integral (2) in position space, but we can also work in momentum space; in fact, as it was detailed in Cerdá-Durán et al. (2004), after simple Fourier algebra, one easily get:

$$\vec{\delta}(\vec{x}_o, \vec{n}) = \frac{2i}{(2\pi)^{3/2}} \int \frac{\vec{k}_\perp}{k^2} F_{\vec{k}}(\vec{n}) e^{-i\vec{k}\vec{x}_o} d^3k , \quad (6)$$

where

$$F_{\vec{k}}(\vec{n}) = \int_{\lambda_L}^{\lambda_0} W(\lambda) B(\lambda) e^{-i\lambda\vec{k}\vec{n}} \delta_{\vec{k}}(\lambda) d\lambda , \quad (7)$$

with $\vec{k}_\perp = \vec{k} - (\vec{n} \cdot \vec{k})\vec{n}$ and $B = -\rho_{m0}/a$.

The n-body simulations are performed using a PM code (Hockney & Eastwood 1988) which was used, tested, and described in detail in Quilis et al. (1998). This code gives function $\delta_{\vec{k}}$ at each time step and, then, for a given vector \vec{n} , the integral of the r.h.s. of Eq. (7) can be performed to get function $F_{\vec{k}}(\vec{n})$. Once this function has been calculated, Eq. (6) is a Fourier transform which gives the deviation $\vec{\delta}(\vec{x}_o, \vec{n})$ corresponding to the direction \vec{n} and to the observer located at point \vec{x}_o ; hence, the deviations associated to all the observers located in the nodes of the Fourier box in position space are simultaneously calculated for a given direction \vec{n} . This information is useful to estimate correlations as it was analyzed in Cerdá-Durán et al. (2004). Similar procedures were used by Aliaga et al. (2002) to study the Rees-Sciama effect in momentum space. In the case of linear scales larger than L_{cut} , the values of $\delta_{\vec{k}}$ necessary to calculate the integral in Eq. (7) are given by the linear approximation to the evolution of density perturbations.

Our U, L and D maps must be statistically analyzed. In order to do that, correlations associated to n directions (or n points on the last scattering surface) are estimated for $n \leq 6$. Given a map of the variable ζ and m directions, the angular correlations are:

$$C_m = \langle \zeta(\vec{n}_1) \zeta(\vec{n}_2) \cdots \zeta(\vec{n}_m) \rangle , \quad (8)$$

where the average is over many maps. Some of these averages are estimated, in next section, for U, L and D maps and for $m \leq 6$. Correlations depend on the relative positions of the chosen directions, namely, they depend on the figures that these directions draw on the last scattering surface. In this paper we have used the sets of directions displayed in Fig. 2, where the basic correlation angle, α , is defined as the angle formed by the two directions of the case $n = 2$. In Gaussian statistics it is well known that (Peebles 1980): (i) all the C_m correlations vanish for odd m and, (ii) for even m , all the correlations can be written in terms of C_2 . Hereafter, these even Gaussian correlations are denoted C_{gm} (the suffix g stands for Gaussian). For the configurations of Fig. 2, one easily obtains the relation:

$$C_{g4}(\alpha) = 2C_2^2(\alpha) + C_2^2(\sqrt{2}\alpha) , \quad (9)$$

leading to $C_{g4}(0) = 3C_2^2(0)$ for $\alpha = 0$, and the equation:

$$\begin{aligned} C_{g6}(\alpha) &= 3C_2^3(\alpha) + 2C_2(\alpha)C_2^2(\sqrt{2}\alpha) + 2C_2(\sqrt{5}\alpha)C_2^2(\alpha) + \\ &+ 4C_2(\alpha)C_2(2\alpha)C_2(\sqrt{2}\alpha) + 2C_2(\sqrt{5}\alpha)C_2^2(\sqrt{2}\alpha) + \\ &+ C_2(\alpha)C_2^2(\sqrt{5}\alpha) + 2C_2(\alpha)C_2^2(2\alpha) , \end{aligned} \quad (10)$$

which takes on the form $C_{g6}(0) = 15C_2^3(0)$ for $\alpha = 0$. Furthermore, according to Bernardeau (1997) and Kesden et al. (2002), if the unlensed maps are assumed to be Gaussian, the non-Gaussian lensed ones have vanishing C_m correlations for odd m values. Our simulated U

maps are almost Gaussian by construction, with small deviations from Gaussianity associated to numerical generation; hence, only these numerical deviations could lead to small odd correlations without any physical meaning. We are not interested in them; Anyway, the correlations C_3 and C_5 have been estimated for the configurations of Fig. 2 and the resulting values have appeared to be compatible with zero. On account of these considerations, the simplest *method to estimate deviations from Gaussianity* is as follows: (a) extract the C_2 , C_4 , and C_6 correlations from the simulated maps, (b) calculate C_{g4} , and C_{g6} functions from C_2 assuming Gaussianity, namely, using Eqs. (9)–(10) and, (c) compare C_4 and C_6 correlations with functions C_{g4} and C_{g6} , respectively.

Now, let us describe the working method used to calculate lens deviations caused by the potential ϕ_1 (scales smaller than L_{cut}). First a preferred direction is fixed and a set of neighbouring directions are chosen to have a uniform pixelisation of a small map of about $2^\circ \times 2^\circ$. This is the crucial point of the method. Afterwards, either Eq. (2) or Eqs. (6)–(7) are solved to get deviations and, finally, these deviations are used to deform U maps of dominant anisotropy. Now, let us look for appropriate values of the box size and resolutions to be used in our PM n-body simulations (ϕ_1 calculation). The angular power spectrum of the lens deformations is expected to be particularly relevant for $\ell > 800$; this means that correlations must be calculated for $\alpha < 0.25^\circ$ and, consequently, the angular size of the simulated maps should be greater than $\sim 1^\circ$. Our map is chosen to be the image of a box face orthogonal to the line of sight of its center and located at the initial redshift; with this choice, photon directions do not spread on many boxes at a given time, and there is no any undesirable effect produced by the spatial periodicity of the fictitious universe under consideration. For this type of maps, the angular size depends on both L_{box} and z_{in} ; it can be easily proved that, in our background universe, for $z_{in} = 5.2$ and $L_{box} = 256 \text{ Mpc}$, the resulting map has a large enough edge of 1.83° . Furthermore, as stated in §1, the separation distance L between the regions crossed by CMB photons in successive boxes is 51.9 Mpc , the number of boxes crossed between redshifts 5.2 and 0. is ~ 30 , and there are hundreds of cluster in the box. Three types of simulations with different resolutions are used in this paper: (i) Low Resolution (LR) simulations involving 128 cells per edge and 128^3 particles, (ii) Intermediate Resolution (IR) simulations using 256 cells per edge and 256^3 particles, and (iii) High Resolution (HR) simulations with 512 cells per edge and 512^3 particles. It is evident that even our HR simulations, with a cell size of 0.5 Mpc and an effective spatial resolution of two cells are not good enough to describe the high density contrasts of core clusters; nevertheless, as it will be discussed in detail in next section, higher resolutions seem to be unnecessary to study the lens deformations of the CMB maps. Fig. 3 shows the column density for particular LR (top), IR (middle), and HR (bottom) simulations. Evidently, structures have developed in the three cases, but they have reached different

levels of evolution. The diffuse figure of the top panel (LR simulation) indicates a low level of evolution (extended structures). The other panels exhibit a better definition because structures have evolved more.

A distance $L = 51.9 \text{ Mpc}$ suffices to deal with clusters and substructures (see §1), but a cutoff eliminating all the scales greater than a maximum one L_{cut} (close to L or smaller than it) is necessary to ensure that photons cross different large scale structures in distinct boxes. Cutoffs at scales L_{cut} of 60 Mpc , 30 Mpc , 15 Mpc and 7.5 Mpc are independently used in next section. A few words about these cutoffs and their consequences are worthwhile. The n-body simulations use all the scales corresponding to the chosen values of L_{box} and Δ (spatial resolution); nevertheless, once the n-body simulation has been developed up to a certain time, any of the mentioned cutoffs can be performed in the peculiar gravitational field responsible for the lens effect (all the scales larger than L_{cut} are thus erased). The n-body particles evolve under the forces associated to the full ϕ field inside the box, whereas the final potential –after the cutoff– is only used to calculate lens deviations using Eq. (2) (or Eqs. (6) and (7)).

In order to perform a certain cutoff, the density contrast, $\delta_{\vec{x}}$, and its Fourier transform, $\delta_{\vec{k}}$ are calculated using n-body simulations and, then the Fourier transform of the total peculiar potential inside the box, $\phi_{\vec{k}}$, is calculated using the Fourier counterpart of Eq. (4): $\phi_{\vec{k}} \propto \delta_{\vec{k}}/k^2$. Afterwards, quantities $\phi_{\vec{k}}$ are avoided for any $k < 2\pi/L_{cut}$ and, finally, an inverse Fourier transform is used to get the peculiar potential ϕ_1 after cutoff. Scales of 60 Mpc , 30 Mpc are larger than the scale $8h^{-1} \text{ Mpc} \sim 11.3 \text{ Mpc}$ and, consequently they are linear, but the scales 15 Mpc and 7.5 Mpc are mildly nonlinear. All these scales are well described in a box having 256 Mpc per edge.

Any cutoff should produce two main effects: (i) it should erase too large spatial scales which are not well described in the n-body simulation, and (ii) the unaltered scales should be small enough to ensure that the CMB photons cross distinct structures in different boxes (along the preferred directions). The erased scales are either linear or mildly nonlinear and, consequently, they can be studied either using the linear approximation to gravitational instability (Bardeen 1980) or applying appropriate techniques as the Zel’dovich approximation (Zel’dovich 1970), the adhesion model (see Sandarin & Zel’dovich (1989) for a review), the lagrangian perturbation approach (Moutarde et al. 1991), and so on; hence, lens deformations produced by scales greater than L_{cut} can be calculated without n-body simulations. Let us now consider the cutoff at $L_{cut} = 60 \text{ Mpc}$. Some scales smaller than 60 Mpc are nonlinear and couple among them and with other scales, the n-body simulation is a good description of the coupled evolution of all these scales. Once the lens effect produced by scales smaller than 60 Mpc has been estimated, the effect produced by strictly linear scales greater

than 60 Mpc (complementary scales) can be analytically or numerically calculated using the linear approximation and then, taking into account that linear scales do not couple among them, and also that these large scales are not expected to be significantly affected by the nonlinear ones (which are much smaller), the resulting effect of the complementary scales can be added to the effect of scales smaller than 60 Mpc to get the total lens deformations. For L_{cut} values much smaller than 60 Mpc , e.g. 7.5 Mpc , all the complementary scales (greater than 7.5 Mpc) are not linear and, furthermore, nonlinear scales smaller and greater than 7.5 Mpc are coupled; these facts lead to a complicate situation. By these reasons, highly linear L_{cut} values, e.g. 60 Mpc , are preferable in order to get the total lens effect, but mildly nonlinear values as 7.5 Mpc can be used to get interesting information (see next section).

In this paper, the lens effect produced by scales smaller than L_{cut} is calculated from an initial redshift $z_{in} \sim 5.2$ to present time. This value of z_{in} seems rather arbitrary, nevertheless, in next section it is proved that, for the scales under consideration, the lensing produced from decoupling to $z = 5.2$ can be neglected.

For $L_{box} = 128 Mpc$, the size of the resulting maps is a little small ($\sim 0.9^\circ$), the number of crossed boxes seems to be too large (~ 60), the L value ($\sim 25 Mpc$) is only marginally admissible to deal with independent clusters in neighbouring boxes (see §1), and the cutoffs must be smaller than $\sim 25 Mpc$; hence, this box size (and similar ones) seems to be a little small. There is only one advantage for $L_{box} = 128 Mpc$: that the cell size of the n-body simulations can be reduced up to 0.25 Mpc , with the same computational cost as in the HR simulations –in boxes of 256 Mpc – used in this paper. In the case of large values $L_{box} \geq 256 Mpc$, a cell size as small as 0.25 Mpc requires too much memory; fortunately, such a high resolution seems not to be necessary to deal with CMB lensing (see §3). On account of these considerations, it seems that $L_{box} = 256 Mpc$ is a good choice to obtain appropriate maps allowing statistical analysis.

Finally, a few words about the calculation of the deviations produced by ϕ_2 ; namely, by the scales greater than $L_{cut} = 60 Mpc$. In this case, a big box of 5000 Mpc is considered with a resolution of $\sim 10 Mpc$ (512 nodes per edge). The potential ϕ_2 created by the linear scales greater than 60 Mpc is calculated, at present time, by using the Fourier counterpart of Eq. (4) and the power spectrum $P(k)$ of the model under consideration (with the normalization $\sigma_8 = 0.9$) and, then, this potential is evolved taking into account that it is proportional to $D_1(a)/a$. The lens effect produced by scales larger than $L_{cut} = 60 Mpc$ is calculated from decoupling ($z_{in} \sim 1100$) to present time. Three of these boxes cover all the photon trajectories from this initial redshift to present time. For an appropriate preferred direction, the distance L is close to 2000 Mpc and, consequently, we can say that, for the scales which produce significant contributions to the lens correlations we are estimating ($\ell > 800$),

photons cross different boxes through distinct linear inhomogeneities. In this case, there is no problem to get a map greater than those of $1.83^\circ \times 1.83^\circ$ associated to the n-body simulations. We can easily obtain a map of deviations having a surface sixteen times greater (hereafter a $7.32^\circ \times 7.32^\circ$ map), which can be superimposed to a mosaic of sixteen $1.83^\circ \times 1.83^\circ$ maps of ϕ_1 deviations to get a large map of total deviations.

3. Results

Two types of maps (hereafter 1 and 2) have been created and analyzed. Type 1 maps are small simulations of the partial lens effect produced by scales smaller than L_{cut} ; among them we can distinguish: U (unlensed), L (lensed) and D (deformation) maps. All these maps have 128×128 nodes and $1.83^\circ \times 1.83^\circ$ (excepting two cases described below). Lens deviations can be calculated with LR, IR and HR simulations and the associated maps are denoted LR-L, LR-D and so on; hence, we have seven sets of maps: the first one is a set of eight hundreds U maps to be deformed by lensing, each of the remaining sets (LR-L, LR-D, IR-L, IR-D, HR-L and HR-D) contains sixteen thousands maps generated by deforming the U maps with the deviations of twenty n-body simulations. Each of these seven sets has been analyzed to get both the averaged angular power spectrum and the mean of the C_m correlations for $2 \leq m \leq 6$ (see §2). Type 2 maps correspond to the lens effect produced by all the scales. Only U (unlensed) and L (lensed) maps (no D maps) are considered in this case. All these maps have 512×512 nodes and $7.32^\circ \times 7.32^\circ$. The U maps are lensed by total lens deviations, in other words, they are lensed by the superimposition of a map of the deviations produced by structures with spatial scales larger than L_{cut} , and a mosaic tiled by sixteen $1.83^\circ \times 1.83^\circ$ small maps of lens deviations produced by scales smaller than L_{cut} . The discontinuities of the mosaic in the edges of the small maps do not significantly affect the estimate of correlations for angular scales $\alpha < 0.25^\circ$, which are much smaller than the size of these small maps.

L maps are deformations of the U maps and, consequently, neither L and U nor D and U maps are statistically independent. According to the relation $L=U+D$ (see §2), the following equation is satisfied:

$$\langle L, L \rangle - \langle U, U \rangle = \langle D, D \rangle + 2\langle D, U \rangle . \quad (11)$$

The l.h.s of this equation is the difference between the C_2 correlations of the L and U maps. The corresponding C_ℓ quantities have a strongly oscillatory character as it was emphasized in Seljak (1996) and Hu (2000) (see also Fig. 5). The same methods used to get the oscillatory form of the solid line of Fig. 5 (from L and U maps), have been also used to get the C_ℓ coefficients of the D maps (associated to the first term of the r.h.s.). The resulting coefficients

do not oscillate (see e.g. Fig. 9). The oscillations associated to the l.h.s. of Eq. (11) are due to the cross correlations of D and U maps appearing in the second term of the r.h.s.

We begin with the analysis of small U and D maps of type 1. This study is performed with the essential aim of testing the method designed in §2 to look for deviations from Gaussianity, this method is used in two opposite situations: almost Gaussian U maps and fully non-Gaussian D maps. For U maps, the question is: can we use the method of §2 to detect small deviations with respect to Gaussianity due to both the map making method and the correlation analysis? The D maps have been considered to verify that large deviations from Gaussianity are easily detected and measured with the same method. For U maps, results are presented in the left panels of Fig. 4. Right panels show deviations from Gaussianity obtained from the HR-D maps. In this Figure, solid lines display correlations directly extracted from the simulated maps, whereas dashed lines show quantities associated to the C_2 correlation function –extracted from the simulated maps– in the case of Gaussian statistics (C_{g4} and C_{g6} in Eqs. (9) and (10)). In the top left panel, the resulting $C_2(\alpha)$ correlation is shown in an appropriate α interval where lens correlations are significant (see the top right panel). The middle (bottom) panels display the ratio $3C_2^2(\alpha)/C_4(\alpha)$ ($15C_3^2(\alpha)/C_6(\alpha)$). The values of these two ratios are unity for a vanishing correlation angle ($\alpha = 0$). Small relative deviations of the dashed (Gaussian statistics) and solid (map statistics) lines of the left panels suggest that the U maps are rather Gaussian by construction. A part of these deviations is associated to the use of small maps. Using more extended maps and a greater total coverage, these deviations decrease because of a smaller sampling variance (a better estimate of C_2 , C_4 , C_6 , C_{g4} and C_{g6}). For a large enough coverage, the residual deviations from Gaussianity would be essentially due to map making (see below). Right panels are the averaged correlations obtained from the HR-D maps. These panels show deviations between solid and dashed lines which are much greater than those of the corresponding left panels; hence, D maps are not Gaussian at all. The ratios presented in the bottom and middle panels are very useful to make well visible –in the figure– the deviations from gaussianity of the U maps (left panels). In the right panels, dashed curves present a singular point where the C_2 correlation of the D maps vanishes (see the top right panel). Very similar results are obtained from LR-D and IR-D simulations. Once it has been verified that, even for small type 1 maps, the method of §2 works, it can be used in other situations.

Let us now analyze L and U maps of type 2. The differences between the correlations of the L and U maps are hereafter called correlation increments. L maps (not D maps) are simplified simulations –without noise, contaminants and so on– of what should be observed in experiments and, consequently, correlation increments (excesses or defects with respect to the theoretical correlations in the absence of lensing) play an important role in order to study whether lensing imprints can be observed in a given experiment. An accurate numer-

ical calculation of the difference between the angular power spectra of L and U maps (C_ℓ increments) is not trivial. There are various numerical problems. In general, the methods designed to extract the C_ℓ coefficients from small maps lead to the worst results in the ℓ intervals where the curvature of the angular power spectrum is great; namely, close to its maxima and minima. The extracted C_ℓ coefficients deviate from their true values in these intervals and the smaller the map the greater these deviations. Furthermore, C_ℓ increments are differences between two similar angular power spectra (which are calculated with numerical techniques leading to small errors) and, evidently, such a subtraction –although possible– could become problematic; however, the C_ℓ coefficients of the D maps (which measure correlations in maps of pure lens deformations) are not either oscillatory quantities or differences between close spectra and, consequently, they can be accurately obtained with small maps and used to do many theoretical and numerical studies about lensing (see below).

The increments of the C_ℓ quantities are exhibited in Fig. 5. As it is well known, the spectrum of the L maps is very similar to that of the U maps and, consequently, C_ℓ increments are small; see Seljak (1996) and Hu (2000) for previous comparisons of L and U angular power spectra. The dotted line of Fig. 5 shows the increments given by the CMBFAST code for the model under consideration. The increments of the solid line are calculated in the following form: (i) sixteen $7.32^\circ \times 7.32^\circ$ U maps are simulated and, then, these maps are deformed with sixteen $7.32^\circ \times 7.32^\circ$ maps of total lens deviations (see above) to get sixteen L maps, (ii) the C_ℓ coefficients of all the U and L maps are numerically obtained; the method used to do that was described in Arnau et al. (2002) and Burigana & Sáez (2003). It is a very efficient method to analyze small uniformly pixelised squared maps, and (iii) the averages of the C_ℓ quantities extracted from L and U maps are subtracted. Solid and dotted lines have the same oscillatory character, but the amplitudes of the maxima and minima are not identical, it is mainly due to the small coverage of the analyzed maps. In fact, it has been verified that the difference between the amplitudes of the dotted and solid lines increases when our study is based on less extended maps. Unfortunately, the use of more extended maps has a great computational cost and it is not necessary in this paper, where the comparison of the dotted and solid lines of Fig. 5 strongly suggest that our numerical methods work. Let us now estimate C_m correlations for even m values greater than two. It is done with the essential aim of analyzing deviations from Gaussianity due to lensing.

In order to estimate the C_m correlations, the sets of directions shown in Fig. 2 are placed at N_c random positions on the map and, in this way, the average of Eq. (8) is performed. For maps with fixed size and resolution, the resulting correlations only depend on: (1) the number N_c , and (2) the accuracy of the interpolation method used to get the temperature contrast in the directions that do not point towards map nodes. On account of these facts, U and L maps of $7.32^\circ \times 7.32^\circ$, with a resolution close to one arcminute, have been analyzed for different

values of N_c and using very distinct interpolation procedures. In this way, it has been verified that, for the two interpolations we have tried (bilinear and splines based on four cells), and for N_c values close to 5×10^5 , the accuracies of the resulting C_2 , C_4 and C_6 correlations are good enough to allow us –using the method of §2– the study and comparison of the deviations from Gaussianity in U and L maps. In order to apply that method, fifty maps of type 2 are analyzed as follows: (a) the averaged C_2 , C_4 and C_6 correlations of the fifty maps are calculated using a certain interpolation method and a selected N_c value, (b) equation (9) is used to get C_{g4} and, (c) the relative differences $\Delta C_4/C_4 = 2(C_4 - C_{g4})/(C_4 + C_{g4})$ are calculated. This analysis is done for U and also for L maps. We begin with the U maps. Typical relative differences resulting from the analysis of an unique U map are of the order of 10^{-2} ; whereas the averaged value corresponding to a few tens of U maps is only of the order of 10^{-3} . It is due to the fact that, as the number of maps increases, the estimation of the correlations is better, and the quantity $\Delta C_4/C_4$ (which vanishes in the Gaussian case) decreases to approach its residual value due to deviations from Gaussianity associated to map making (see above). By comparing the averaged values corresponding to thirty, forty and fifty U maps, it has been verified that the $\Delta C_4/C_4$ ratio is close to 10^{-3} in all the cases. The same values of $\Delta C_4/C_4$ are obtained for the two interpolation methods and also for N_c values greater than 5×10^5 . The bottom panel of Fig. 6 describes the same study as in the top one, but the involved correlations are now C_6 and C_{g6} . Results are similar. All these results strongly suggest that the $\Delta C_4/C_4$ and $\Delta C_6/C_6$ averaged values corresponding to fifty U maps (solid lines of the top and bottom panels of Fig. 6, respectively) measure actual deviations from Gaussianity due to map making. Fifty L maps have been obtained from the chosen U maps by using independent realizations of lens deviations. These maps have been analyzed in the same way as the U maps. It has been verified that for thirty, forty and fifty L maps, the resulting $\Delta C_4/C_4$ and $\Delta C_6/C_6$ values are always around 20 % greater than those of the U maps. This percentage is almost independent on the interpolation procedure for any N_c value greater than 5×10^5 . The dotted lines of the top and bottom panels of Fig. 6 shows $\Delta C_4/C_4$ and $\Delta C_6/C_6$ relative differences obtained from fifty L maps. Independent lens deviations have deformed the U maps in such a way that the $\Delta C_4/C_4$ and $\Delta C_6/C_6$ quantities of the resulting L maps systematically exceed those of the U maps. These quantities measure the excess of non-Gaussianity in the L maps beyond what is seen in the U maps. All these results strongly suggest that, although deviations from Gaussianity produced by lensing are only ~ 20 % of those introduced in the U maps by the map making procedure, this ~ 20 % can be pointed out with the method of §2.

Instead of numerical deviations from Gaussianity associated to map making, observation maps involve other deviations due to galactic contaminants, the Sunyaev-Zeldovich effect (Cooray 2001), and so on, which are coupled to lens deviations from Gaussianity. Before any

eventual separation of the different deviations from Gaussianity appearing in observation maps: each contribution and its possible cross correlations with the remaining ones must be characterized, including lens contribution we are analyzing here.

Let us now return to the analysis of small type 1 maps with the essential aim of justifying that the initial redshift for lensing calculations ($Z_{in} = 5.2$) and the resolution of the N-body simulations have been appropriately chosen. In order to do that, we study both the contribution of the different spatial scales to lens deformations of the CMB and the time variation of these contributions. Results are presented in Fig. 7. In order to do such a study, scales larger than $L_{cut} = 60 \text{ Mpc}$ (top panels), $L_{cut} = 30 \text{ Mpc}$ (middle panels), and $L_{cut} = 15 \text{ Mpc}$ (bottom panels), have been erased in the peculiar gravitational potential and, in each of these three cases, the D maps and their C_ℓ quantities have been calculated from $z_{in} = 5.2$ to redshifts 3.9 (pointed-dashed lines), 2.6 (dashed lines), 1.3 (pointed lines) and 0. (continuous lines). Left, central and right panels correspond to an arbitrarily chosen LR, IR and HR n-body simulation. In all the panels, the angular power spectrum increases with the redshift and it is very small at $z = 3.9$; hence, for the scales under consideration, an initial redshift of 5.2 is a very good choice, and negligible lens deviations are expected at $z > 5.2$. Furthermore, the most important part of the effect is produced between redshifts 1.3 and 0 (compare solid and pointed lines in all the panels). In any panel (fixed cutoff and simulation), the maxima of the curves shift to right as the redshift increases. It is due to the fact that the angle subtended by the involved scales depends on the redshift. Since this angle (ℓ) is a decreasing (increasing) function of the redshift, the maxima shift to right. For a given redshift, the curves of the middle panels are shifted to right (left) with respect to those of the top (bottom) panels. It is due to the fact that –as a result of the cutoff– the scales of the middle panels are smaller (greater) than those of the top (bottom) one and, consequently, they subtend a smaller (greater) angle for a fixed redshift. From the comparison of the continuous lines in the top and middle panels it follows that spatial scales between 60 and 30 Mpc , whose effects are (are not) included in the top (middle) panel, are responsible for the most important part of the total effect (solid line of the top panel). Similarly, the comparison of the solid lines of the middle and bottom panels indicates that the effect produced by the scales between 30 and 15 Mpc is greater than that produced by the scales smaller than 15 Mpc in all the cases. This last effect due to scales smaller than 15 Mpc is very small for LR simulations (left bottom panel), but a comparison of the bottom panels –in which the n-body resolution increases from left to right– among them lead to the conclusion that this effect of scales smaller than 15 Mpc grows as the n-body resolution increases. It is due to the fact that the greater the n-body resolution the greater the growing of the scales smaller than 15 Mpc . In the case of the HR simulation of the right panels of Fig. 7, a cutoff at 7.5 Mpc has been also performed. Results are presented in Fig. 8 (same structure as Fig. 7),

where we see that the amplitude of the effect produced by scales smaller than 7.5 Mpc is much smaller than that produced by the complementary scales (up to 60 Mpc). Of course, this effect should increase as resolution does, nevertheless, for the angular scales of interest, this effect would be negligible –for any resolution– as compared with that of the remaining scales. From the above considerations, it follows that the most significant scales are greater than 15 Mpc in all cases. Fortunately, these scales are rather well described by our LR and IR simulations and, consequently, no important differences appear among the averaged spectra of our LR-D, IR-D and HR-D maps. These spectra are presented in Fig. 9, where we see that, for great enough ℓ values, the larger the n-body resolution the greater the resulting C_ℓ quantities. These ℓ values correspond to angles subtended by small enough spatial scales which grow more as resolution increases. We see that LR simulations suffice to get a very good approach to the angular power spectrum of lens deformations.

Twenty LR simulations have been used in our study. Each of these simulations leads to eight hundred D maps which can be analyzed to get an averaged angular power spectrum; in this way, twenty different power spectra appear whose mean has been represented in the solid line of Fig. 9. We are now interested in the distribution of these twenty spectra around the mean spectrum of Fig. 9. How much separated are these spectra from their mean? In order to answer this question, the mean and variance of the twenty C_ℓ coefficients have been calculated for every ℓ value and, afterwards, mean, mean plus variance, and mean minus variance have been used to built up solid, dotted and dashed lines of the top panel of Fig. 10, which gives a good idea about the dispersion of the spectra associated to each of the twenty LR simulations. The middle (bottom) panel of Fig. 10 has the same structure as the top one, but it corresponds to IR (HR) simulations.

Since a LR simulation suffices to get a rather good description of CMB lensing, we have developed a new LR simulation in a box of 512 Mpc (256^3 cells and 256^3 particles) using: (i) a cutoff at 60 Mpc , (ii) fifteen boxes to cover the photon trajectories from $z_{in} = 5.2$ and, (iii) a preferred direction leading to a separation distance $L = 103.8 \text{ Mpc}$. Evidently, the situation is better than in previous simulations because of the smaller value of the number of boxes and the larger values of L and L_{box} . Since the box size is twice that of previous simulations, the new L and D maps are greater than those we have already analyzed, they have 3.66° degrees per edge. New U maps have been built up in concordance with the new coverage. In the top panel of Fig. 11, we show the spectra of the resulting D maps at redshifts 3.9, 2.6, 1.3, and 0. (same format as in Figs. 7 and 8). The spectrum is very similar to those obtained with previous LR simulations (compare with the top left panel of Fig. 7 taking into account that we are considering the spectra of two particular LR simulations). These results strongly suggest that boxes of 256 Mpc are large enough to study CMB lensing.

Results obtained from Eq. (2), in position space, are now compared with those obtained, in momentum space, from Eqs. (6) and (7) (plus statistics based on 128^3 observers, see §2). In order to do this comparison, LR simulations as those used along the paper (excepting previous paragraph) are considered. The cutoff is performed at $60 Mpc$. The main difference with respect to previous cases is the size and resolution of the simulated D maps. We have not been able to work with 128×128 directions –in momentum space– as a result of the high computational cost of the method based on Eqs. (6) and (7), which works with 128^3 observers at the same time. By this reason and with the essential aim of comparing results in position and momentum spaces, regular maps covered by 16×16 directions with a resolution of $5'$ and an edge of 1.25° have been simulated. Size and resolution are smaller than in previous cases and, consequently, only some C_ℓ quantities can be extracted from the new D maps with admissible accuracy. In any case, the D maps can be simulated using the two methods and identical U maps; afterwards, the C_ℓ coefficients can be extracted using the same codes and, finally, results can be compared. The solid line of the bottom panel of Fig. 11 shows the spectrum obtained, in position space, by averaging the spectra of twenty D maps with the new size and resolution. Dashed and dotted lines exhibit the C_ℓ quantities found, in momentum space, using only one LR simulation in each case, but considering 128^3 observers in the statistical analysis (see Cerdá-Durán et al. (2004) and §2). Figure 11 shows that both methods lead to similar curves. If we average over twenty simulations in momentum space, the final spectrum is close to that displayed in the solid line of Fig. 11; namely, both methods lead to similar final spectra separately.

4. Discussion and conclusions

A method for ray-tracing through n-body PM simulations (Cerdá-Durán et al. 2004) is used to simulate lensed maps of the CMB. Our attention is focused on the study of deviations from Gaussianity in these maps. Some correlation functions as C_4 , C_6 , C_{g4} and C_{g6} are estimated and compared –for the first time– to measure deviations from Gaussianity. Considerable emphasis is put on the comparison of the lens deformations produced by different small spatial scales, and also in the study of the evolution of these deformations.

For a given map, the relative difference between the correlation functions C_4 and C_{g4} , and also between C_6 and C_{g6} measure deviations from Gaussianity. These relative differences $-\Delta C_4/C_4$ and $\Delta C_6/C_6$ have been calculated for U and L maps. According to our expectations, the functions $\Delta C_4/C_4$ and $\Delta C_6/C_6$ of the U maps take on small values pointing out small deviations from Gaussianity due to construction (see §3). This success in the analysis of U maps strongly suggest that the same method could be applicable to the analysis of other

deviations from Gaussianity (lensing, Sunyaev-Zelovich and so on). In the case of L maps, quantities $\Delta C_4/C_4$ takes on values which are greater than the values of the U maps. The same occurs for $\Delta C_6/C_6$. The differences between the $\Delta C_4/C_4$ ($\Delta C_6/C_6$) quantities of the L and U maps are about the twenty per cent of the $\Delta C_4/C_4$ ($\Delta C_6/C_6$) values corresponding to the U maps. The same values of these differences are obtained for different interpolation procedures and whatever the value of the parameter $N_c > 5 \times 10^5$ may be; hence, these differences measure actual deviations from Gaussianity produced by lensing (see discussion in §3).

L and U maps lead to very similar C_ℓ quantities. Differences between these quantities are calculated with CMBFAST and also from the analysis of our simulated maps. These differences are displayed in Fig. (5). Both methods lead to comparable results. This fact strongly support the ray-tracing procedure, the numerical simulations, and the correlation analysis used in this paper.

Box sizes of $\sim 256 Mpc$ seem to be appropriate for ray-tracing through n-body simulations. Much greater (smaller) sizes lead to problems with resolution (L values, number of boxes and so on). In these boxes, scales between 15 and 60 Mpc –small enough as compared with chosen box size– produce the largest part of the lens effect on the CMB, whereas scales smaller than 15 Mpc only produces a small part. By this reason, low resolution n-body simulations suffice to get a good approximation to the angular correlations produced by lensing. For scales smaller than 60 Mpc , the most important part of the lens effect is produced between redshifts 2.6 and 0., whereas only a small part of this effect is produced at $z > 3.9$.

Two independent codes based on distinct approaches have been used to deal with the same problem: the estimate of lens correlations produced by scales smaller than L_{cut} . One of these codes works in momentum space and involves many observers (Cerdá-Durán et al. 2004) for statistical analysis. In the second code, calculations are performed in position space –method applied along this paper– and the observer is unique. Both codes lead to very similar angular power spectra after averages.

Let us now list some prospects. It would be worthwhile: (1) the use of other n-body codes (allowing more resolution) with the essential aim of getting more accurate correlations at small angular scales, (2) the application of appropriate modern methods (wavelets, Minkowski functionals and so on) to study deviations from Gaussianity in the L and U maps we have simulated, (3) the characterization of all the deviations from Gaussianity which appear coupled in observation maps, e.g. deviations due to the Sunyaev-Zel'dovich effect, to the radiation from the galaxy in the CMB frequencies and so on. The necessary statistical analysis could be developed by using either the method of this paper or other methods (see

above), and (5) the study of the possible detection of deviations from Gaussianity in maps of the PLANCK mission.

REFERENCES

- Aliaga, A.M., Quilis, V., and Sáez, D. 2002, MNRAS, 330, 625
- Arnau, J.V., Aliaga, A.M., and Sáez, D. 2002, A&A, 382, 1138
- Bardeen, J.M. 1980, Phys. Rev. D, 22, 1882
- Bennet, C.L. et al. 2003, ApJS, 148, 1
- Bernardeau, F. 1997, A&A, 324, 15
- Burigana, C., and Sáez, D. 2003, A&A, 409, 423
- Cerdá-Durán, P., Quilis, V., and Sáez, D. 2004, Phys. Rev. D, 69, 043002
- Cooray, A. 2001, Phys. Rev. D, 64, 063514
- Fullana, M.J., and Sáez, D. 2000, New A, 5, 109
- Hockney R.W., and Eastwood J.W. 1988, Computer Simulations Using Particles (Bristol: IOP Publisings)
- Hu, W. 2000, Phys. Rev. D, 62, 043007
- Jain, B., Seljak, U., and White, S. 2000 ApJ, 530, 547
- Kesden, M., Cooray, A., and Kamionkowski, M. 2002, Phys. Rev. D, 66, 083007
- Martínez-González, E., Sanz, J.L. and Silk, J. 1990, ApJ, 355, L5
- Moutarde, F., Alimi, J.-M., Bouchet, F.R., Pellat, R., and Ramani, A. 1991, ApJ, 382, 377
- Peebles, P.J.E. 1980, The Large Scale Structure of the Universe, Princeton Univ. Press, Princeton
- Quilis, V., Ibáñez, J.M., and Sáez, D. 1998, ApJ, 502, 518
- Sáez, D., Holtmann, E., and Smoot, G.F. 1996, ApJ, 473, 1
- Sandarin, S.F., and Zel'dovich, Ya. B., 1989, Rev. Mod. Phys., 61, 185

Seljak, U., and Zaldarriaga, M. 1996, ApJ, 469, 437

Seljak, U. 1996, ApJ, 463, 1

White, M., and Hu, W. 2001, ApJ, 537, 1

Zel'dovich, Ya. B., 1970, A&A, 5, 84

This work has been supported by the Spanish MCyT (project AYA2003-08739-C02-02 partially funded with FEDER) and also by the Generalitat Valenciana (grupos03/170). PC-D thanks the Ministry of Science and Technology for a fellowship. Calculations were carried out at the Centro de Informática de la Universidad de Valencia (CERCA and CESAR).

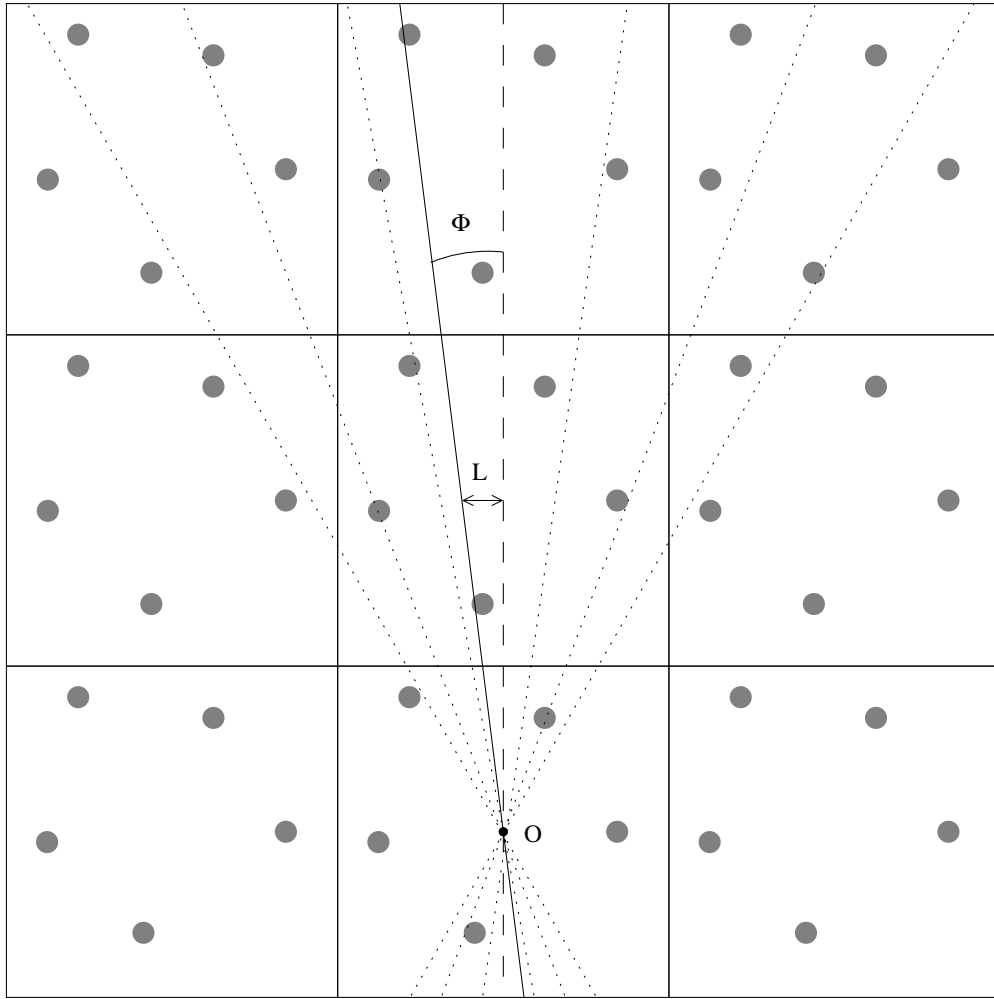


Fig. 1.— Sketch of a 2D universe covered by squared patches. Circles are structures, the observer is located at point O and lines are photon trajectories

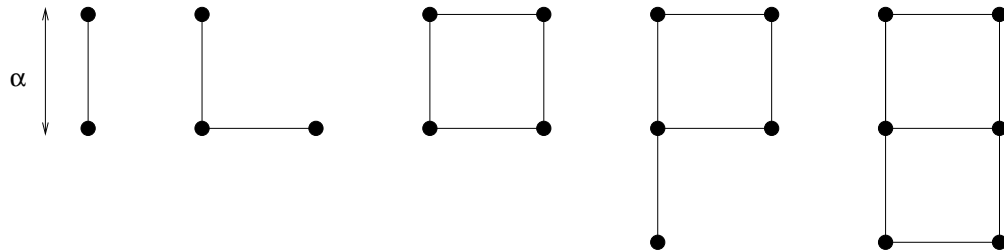


Fig. 2.— Configurations of n directions for $2 \leq n \leq 6$. The sets of n directions draw these Figures on the Last Scattering Surface.

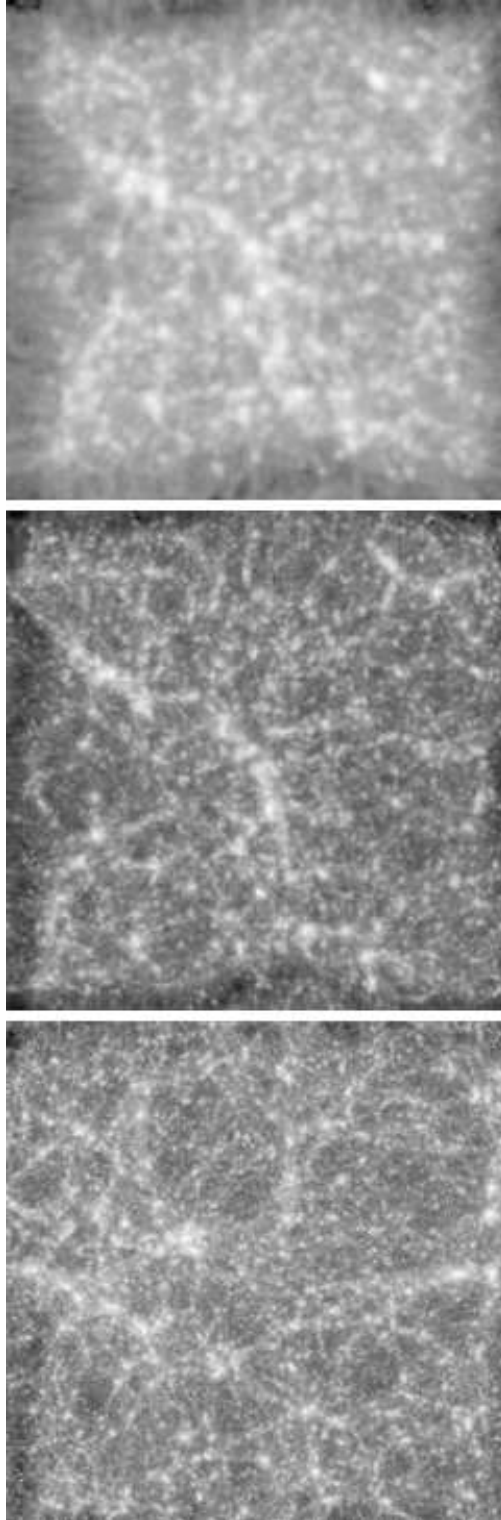


Fig. 3.— integrated column density along an edge of the simulation box. Top, middle and bottom panels correspond to a LR, IR and HR simulation, respectively.

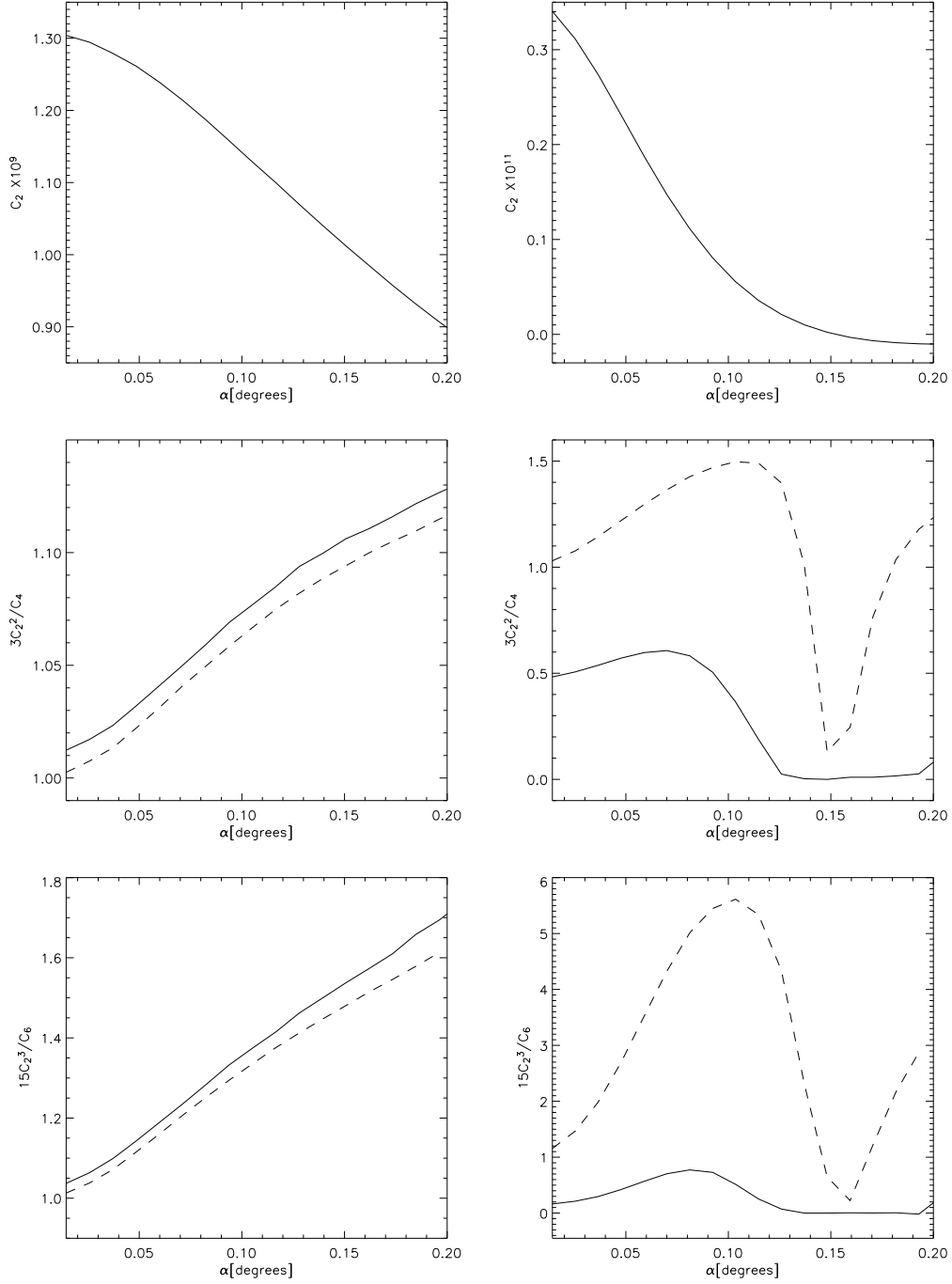


Fig. 4.— Left (right) panels correspond to U (D) maps. Top, middle and bottom panels exhibit functions C_2 , $3C_2^2(\alpha)/C_4(\alpha)$ and $15C_2^3(\alpha)/C_6(\alpha)$ against the correlation angle α in degrees. In the solid lines, correlations C_2 , C_4 , and C_6 are directly extracted from the maps, whereas the ratios shown in the dotted lines are calculated using the Gaussian correlation C_{g4} and C_{g6} defined in the text. The separation between continuous and dotted lines measure deviations from Gaussianity.

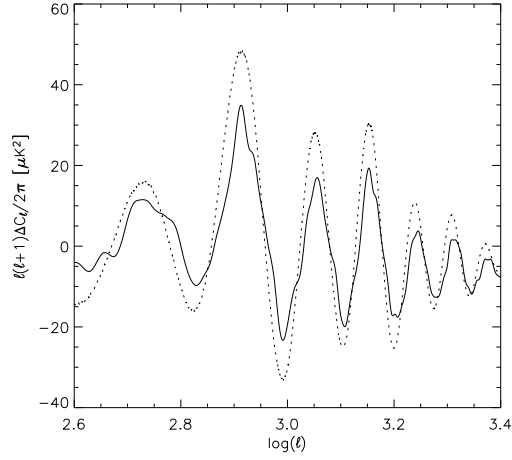


Fig. 5.— Difference ΔC_ℓ in μK^2 , multiplied by the factor $\ell(\ell + 1)/2\pi$, *v.s.* $\log \ell$. Difference is calculated between the C_ℓ coefficients of L and U maps. Dotted line has been obtained with CMBFAST and solid line from the numerical analysis of sixteen $7.32^\circ \times 7.32^\circ$ L and U maps (see the text).

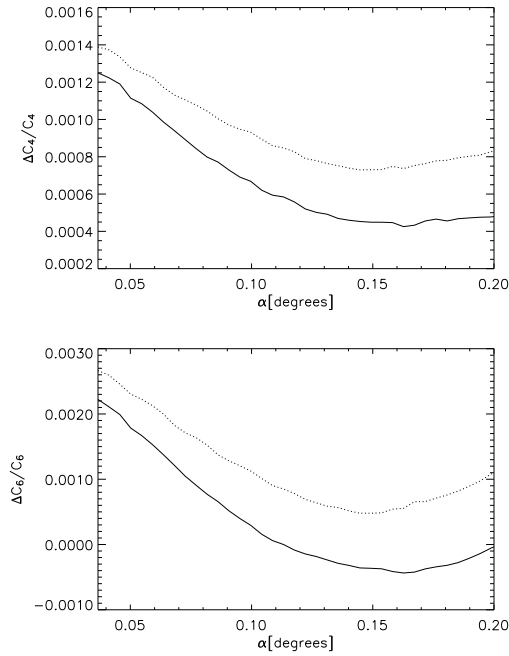


Fig. 6.— Top panel shows relative differences $\Delta C_4/C_4$ between the C_4 correlations extracted from the U maps and the C_{g4} Gaussian correlations (see text), *v.s.* the correlation angle in degrees. Bottom panel has the same structure as the top one, but it exhibits relative differences $\Delta C_6/C_6$.

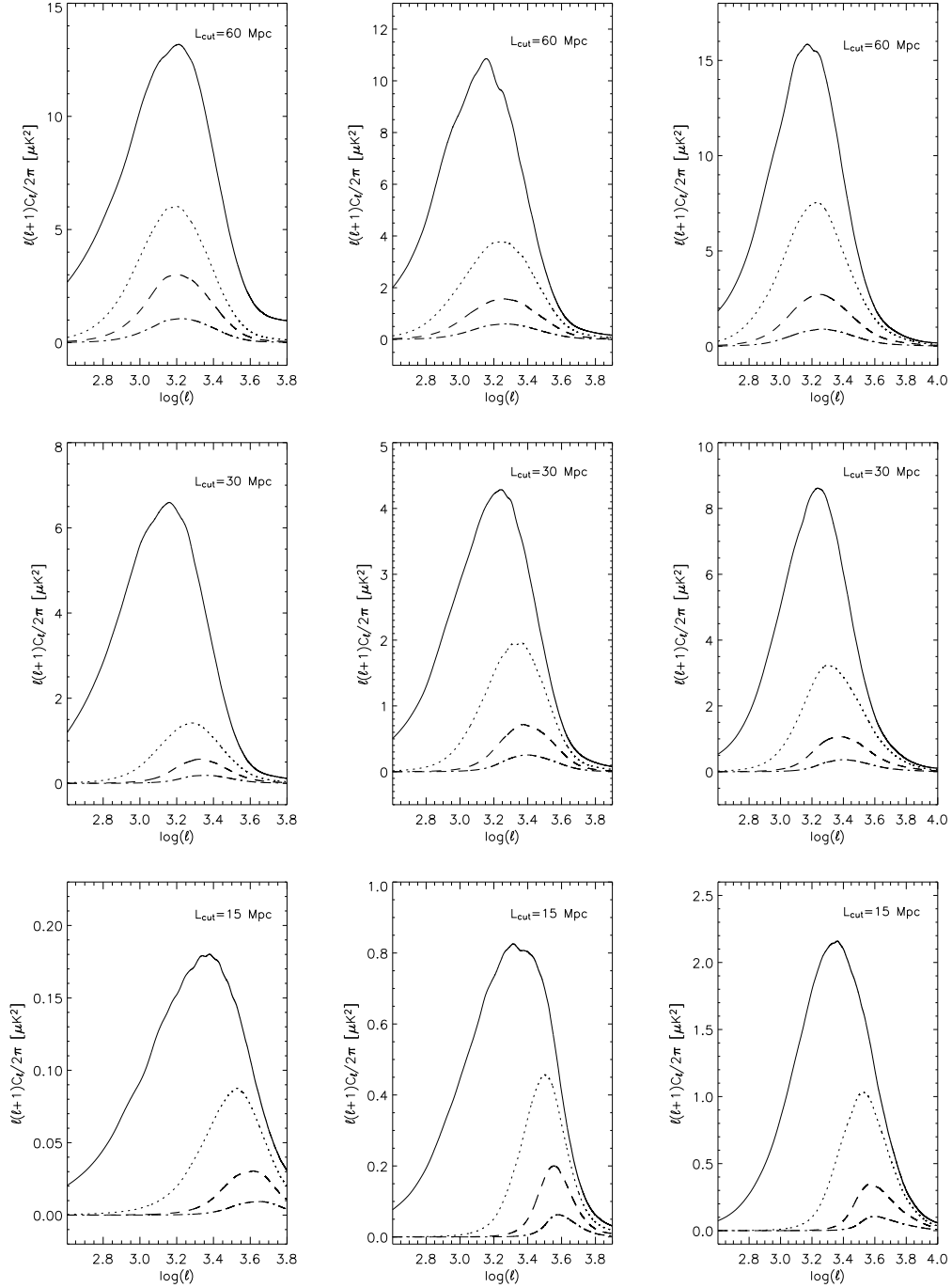


Fig. 7.— Quantity $\ell(\ell + 1)C_\ell/2\pi$ in μK^2 *v.s.* $\log \ell$. Left, central and right panels involve LR, IR and HR simulations. Top, middle and bottom panels correspond to L_{cut} values of 60, 30, and 15 *Mpc*. Solid, pointed, dashed, and pointed-dashed lines display the C_ℓ coefficients of the D maps produced by lensing between $z_{in} = 5.2$ and the redshifts 3.9, 2.6, 1.3, and 0., respectively.

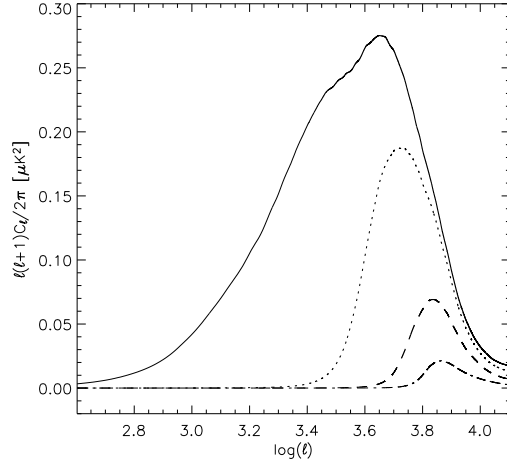


Fig. 8.— Same as in Fig. 7 for the HR simulation of that Figure (right panels), with a cutoff at $L_{cut} = 7.5 Mpc$

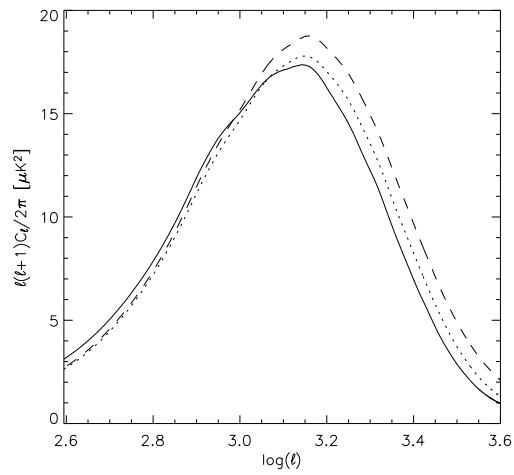


Fig. 9.— Quantity $\ell(\ell + 1)C_\ell/2\pi$ in μK^2 *v.s.* $\log \ell$. The C_ℓ coefficients involved in the solid, dotted and dashed lines correspond to the averaged power spectra of the sets of maps LR-D, IR-D and HR-D defined in the text

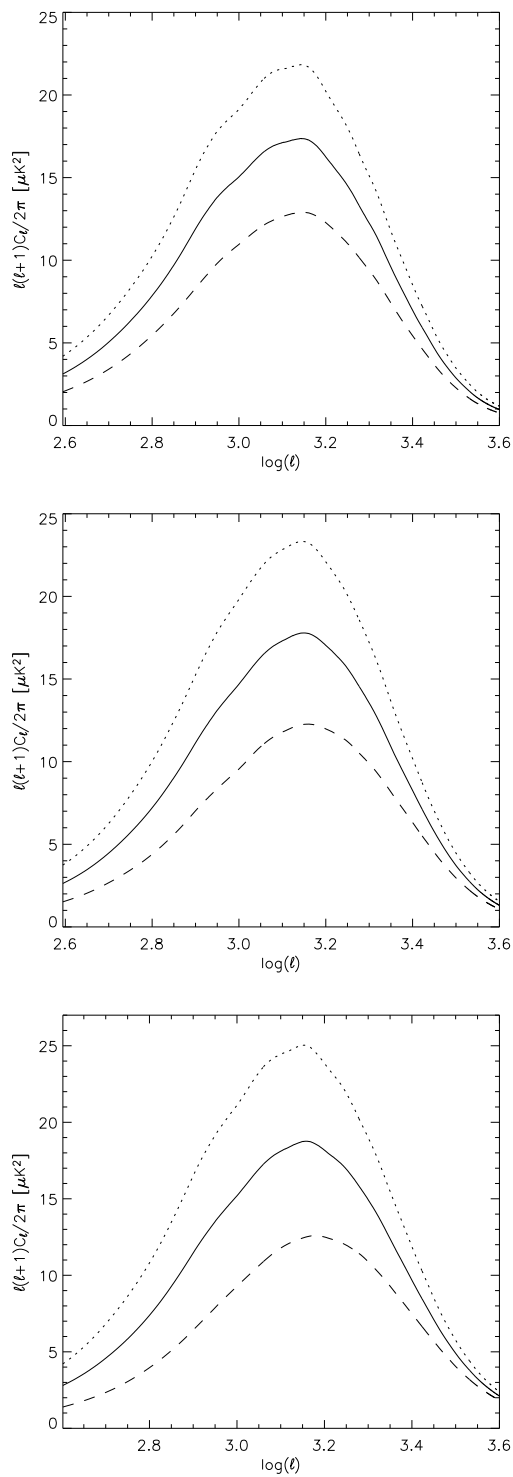


Fig. 10.— Quantity $\ell(\ell + 1)C_\ell/2\pi$ in μK^2 *v.s.* $\log \ell$. Top, middle and bottom panels show results from LR, IR and HR simulations. Solid lines are the averaged spectra displayed in Fig. 9, whereas the dotted and dashed lines show 1σ curves in the spectra distribution (see the text for more details).

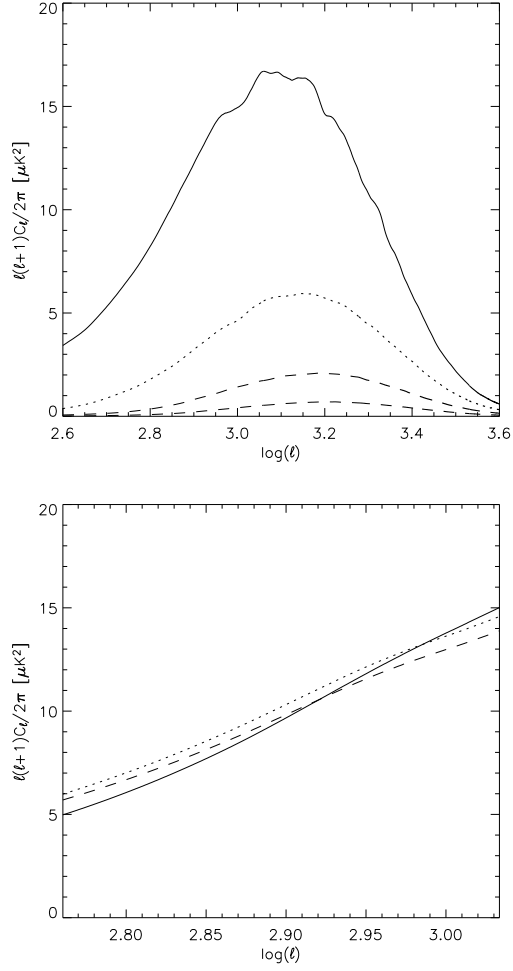


Fig. 11.— Top panel has the same structure as panels of Fig 7. It corresponds to a LR simulaton in a big box of $512 Mpc$, with a cutoff at $L_{cut} = 60 Mpc$. Bottom panel represents the same function as in the top one, but the C_ℓ coefficients have been obtained from D maps with a size of 1.25° and a resolution of $5'$. The C_ℓ quantities of the solid line correspond to a map obtained from Eq. (2) in position space, whereas in the dotted and dashed lines, we present the C_ℓ coefficients of a map, which has been found from Eqs. (6) and (7) in momentum space (see the text for more explanations).